Macroscale damage model calibrated from discrete mesoscale data with a consistent description of fracture

Julien Khoury, Gilles Pijaudier-Cabot, Gianluca Cusatis

European Journal of Mechanics / A Solids 118 (2026) 106115

Contents lists available at ScienceDirect

European Journal of Mechanics / A Solids

journal homepage: www.elsevier.com/locate/ejmsol

Full length article

Macroscale damage model calibrated from discrete mesoscale data with a consistent description of fracture☆

Julien Khoury [a], Gilles Pijaudier-Cabot [a,*], Gianluca Cusatis [b]

[a] Universite de Pau et des Pays de l'Adour, CNRS, LFCR, Anglet, France
[b] Northwestern University, Department of Civil and Environmental Engineering, Evanston IL, United States

ARTICLE INFO

Keywords:
Lattice discrete particle model
Continuum-based models
Coarse graining
Multiscale
Nonlocal damage

ABSTRACT

This study shows that nonlocal models for fracture can be calibrated from field data, e.g., strain fields, stress and other internal variable fields, including their internal length. There is no need to consider specimens of various geometries or size effect data. However, such a calibration should be performed with caution as the fracture process zone ought to be well described. This work starts from a discrete model (LDPM) viewed as a high-fidelity model, and uses it to generate a synthetic data set for the calibration of a macroscale damage model. Compared to the methodology where the internal length and material parameters are obtained from fitting field data altogether, the present study shows that constraining the internal length in the nonlocal model to fit the width of the FPZ prior to calibration yields more accurate results. Consistent structural responses and correct size effects predictions are obtained.

1. Introduction

Crack propagation is typically the cause of failure in quasi-brittle materials under limited triaxial compression. Micro-cracking gradually occurs in what is called the Fracture Process Zone (FPZ) prior to forming the main crack. In notched bending beams for instance, the FPZ can be a relatively wide area ahead of the crack tip and the width of this zone is directly related to the heterogeneities of the material (Haidar et al., 2005).

One way to model such a progressive cracking is through the use of Continuum Damage Mechanics (CDM). A simple version of such a model involves a scalar damage parameter that reduces Young's modulus of the material (see e.g., Mazars and Pijaudier-Cabot 1989). It is this version of a continuum damage model which will be considered in this contribution, keeping in mind that more sophisticated damage-based models might be more accurate (see e.g., Desmorat et al. 2007).

The scalar damage model has been shown to capture tensile failure of concrete, including size effect. An internal length needs to be inserted in the constitutive model to cope with strain softening and the inherent difficulties related to strain and damage localization, namely to avoid failure with vanishing energy dissipation. This is performed by considering that the variable controlling the growth of damage is a spatial average in the nonlocal integral model (Pijaudier-Cabot and Bažant, 1987), or equivalently it is the solution of a Fredholm equation in the gradient damage model (Peerlings et al., 1996). This internal length relates the constitutive properties to the fracture energy of the material. Other regularized models, such as phase field models (Heinzmann et al., 2024; Miehe et al., 2010; Feng and Wu, 2018) or peridynamic models (see e.g., Silling and Askari 2005, Silling et al. 2007) also incorporate an internal length which should be viewed as a regularization parameter (i.e., see Pijaudier-Cabot et al., 2024 for such a discussion in the case of peridynamics). The foregoing considerations could also very well apply to these.

Adding an internal length means that this parameter needs to be calibrated from experiments, in addition to the other model parameters. In a local approach, the internal length is replaced by the characteristic size of the finite elements and the softening parameters are adapted so that the energy dissipated upon failure is consistent with the fracture energy (La Borderie, 2003; Arruda et al., 2022). In a nonlocal approach, the calibration requires data that trigger the spatial correlation due to nonlocality. This may be obtained, for instance, from size effect tests on geometrically similar specimens (Le Bellégo et al., 2003) or from full-field displacement or strain data, in addition to classical force vs. displacement responses. Some attempts to calibrate a damage model from experiments with digital image correlation (DIC) can be found in the literature (see Geers et al. 1999), but the internal length was not coupled to the fitting procedure, carried out on a restricted area of the sample tested. A complete calibration method (including the fracture energy and the regularization length) of a phase field model for

☆ This article is part of a Special issue entitled: 'Jean Lemaitre' published in European Journal of Mechanics / A Solids.

* Corresponding author.
E-mail address: gilles.pijaudier-cabot@univ-pau.fr (G. Pijaudier-Cabot).

https://doi.org/10.1016/j.euromechsol.2026.106115
Received 22 August 2025; Received in revised form 17 March 2026; Accepted 18 March 2026
Available online 25 March 2026

fracture has been performed, based on DIC by Kosin et al. (2024). Still, calibration of constitutive models for failure from full fields resulting from digital image analysis of experiments remains rather scarce in the literature, at least for concrete. A feasibility of such a calibration process may be considered using synthetic full fields (displacement, strain, stress) resulting from discrete models (Védrine et al., 2025).

Recently, Pijaudier-Cabot and co-workers (Khoury et al., 2026) have used a high-fidelity mesoscale, lattice discrete, model to generate synthetic full-field data sets, from which a nonlocal CDM model was calibrated. Synthetic data sets may provide supplementary information in addition to experimental data, such as the stresses needed to perform calibration. Further, synthetic datasets may also provide information regarding a large spectrum of loading histories involving material failure for which experimental data are lacking. However, the mesoscale model should provide for this purpose local and global responses with a high-fidelity description of experiments.

Lattice discrete models are widely used in the field of fracture mechanics (Bolander et al., 2021). In these models, the microstructure of the material is explicitly represented, and the overall mechanical behavior results from interactions between discrete particles connected by nonlinear bonds. First developed by Cusatis and colleagues (Cusatis et al., 2011), the lattice discrete particle model (LDPM) is a mesoscale model designed to simulate particle interactions in cohesive granular materials such as fiber-reinforced concrete and mortar (Rezakhani et al., 2021; Schauffert and Cusatis, 2012), or concrete (Zhu et al., 2022). LDPM has demonstrated in many instances superior prediction capabilities (see e.g., Pathirage et al. 2023, Lyu et al. 2023), which is the reason why it is considered here as a high-fidelity model.

In discrete or mesoscale models, displacements are solved, but stresses and strains in their tensorial form are not be defined. An intermediate step is needed, which converts the discrete displacement field into a strain field, and the inter-particle forces into stresses, prior to performing calibration of a macroscale constitutive response using such full field quantities. A suitable technique for this purpose is coarse graining (Eid et al., 2021) but in this process, a coarse graining length appears, and it needs to be calibrated. In Khoury et al. (2026), the coarse graining length was determined in the elastic regime, by constraining the coefficient of variation of the upscaled (stress) field to be less than a fixed tolerance in the case of uniaxial loading.

It is important to remark that the calibration problem involves now two lengths: (1) the coarse graining length related to the fluctuations of averaged mesoscale quantities – it is directly connected to the size of the representative volume element; and (2) the material internal length – it defines the size of the FPZ. The possible interactions between these two lengths, related to the mesostructure of the heterogeneous material is also an issue that this paper intends to address.

In Khoury et al. (2026), the calibration of a damage model performed from LDPM local fields computed from notched bending beams yielded a unique set of model parameters and the internal length turned out to be close to the coarse graining length. As we will see, this approach overestimates the size of the FPZ which turns out to be much larger than that observed in LDPM computations. This overestimation of the size of the FPZ has severe consequences: when trying to predict size effect, which is one of the test cases for evaluating the accuracy of constitutive relations (Bažant and Nguyen, 2023), it introduces a bias. Additionally, when considering multiphysics where material damage induces changes in transport properties such as permeability, an overestimated size of the FPZ may yield very different responses to environmental loads. This paper tries to resolve this issue: the calibration procedure is reconsidered by constraining the internal length to yield a FPZ size close to that of LDPM.

After recalling the background and illustrating the motivation of this study, Section 3 discusses a modified calibration method, where the internal length is first fitted to provide a correct size of the FPZ, and then the coarse graining length is derived from the fitting of local stress and strain fields. By constraining the model to capture the width of the FPZ properly, better predictions of the size effect on bending beams are achieved. Section 4 provides additional validation studies on different geometries.

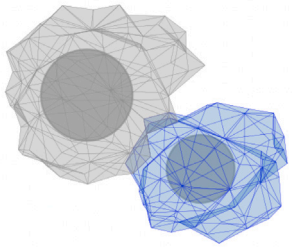

Fig. 1. Polyhedral Cells Surrounding the LDPM Grains.

2. Background

This section begins by recalling the basic ingredients of the mesoscale model, the coarse graining technique and the damage model which will be calibrated.

2.1. The lattice discrete particle model

LDPM is used here to model concrete as a heterogeneous material, more details can be found in Cusatis et al. (2011). In LDPM, grains are represented by spherical particles of various sizes, according to their size distribution. To avoid the description of fine aggregate, a cut-off is applied on this distribution and typically, grains with a size larger or equal to 0.5 times the maximum aggregate size are represented only. The others are mixed with the cement paste, forming the glue located in between the grains. Nodes are placed at the center of each individual particle. The lattice system is generated by performing a Delaunay tetrahedralization. The domain is then tessellated so that each spherical particle is surrounded by a network of polyhedral cells, as shown in Fig. 1. Triangular facets form the surface of each polyhedral cell, and stresses and strains are expressed in vector form on these facets.

LDPM uses constitutive equations defined at the level of facets to model tensile fracturing with strain softening, cohesive and frictional shearing, and compressive behavior with strain hardening. Since this study focuses only on concrete fracturing, the relevant constitutive laws are recalled only. If $\mathbf{x}_i$ and $\mathbf{x}_j$ represent the positions of nodes i and j adjacent to facet k, the strain vector for the facet is defined in Eq. (1), where e_{N_k} is the normal strain component, e_{M_k} and e_{L_k} are the tangential strain components, $[[\mathbf{u}_k]] = \mathbf{u}_j - \mathbf{u}_i$ is the displacement jump corresponding to facet k, $l_k = |\mathbf{x}_j - \mathbf{x}_i|$ is the distance between the two nodes, $\mathbf{n}_k = (\mathbf{x}_j - \mathbf{x}_i)/l_k$ is the unit vector in the direction of the facet, and $\mathbf{m}_k$ and $\mathbf{l}_k$ are two mutually orthogonal unit vectors in the facet plane orthogonal to the line connecting the adjacent nodes.

$$\mathbf{e}_k = [e_{N_k}\ e_{M_k}\ e_{L_k}]^t = \left[\frac{\mathbf{n}_k^t[[\mathbf{u}_k]]}{l_k}\ \frac{\mathbf{m}_k^t[[\mathbf{u}_k]]}{l_k}\ \frac{\mathbf{l}_k^t[[\mathbf{u}_k]]}{l_k}\right]^t \tag{1}$$

In the remaining, subscript k will be dropped for the sake of clarity. The elastic behavior is described in Eq. (2):

$$t_N = E_N e_N, t_M = E_T e_M, t_L = E_T e_L \tag{2}$$

t_N represents the normal component, and t_M and t_L are the shear components, $E_N = E_0$ and $E_T = \alpha_0 E_0$. The effective normal modulus E_0 and the shear-normal coupling parameter α_0 define the elastic response.

An effective strain $e = \left(e_N^2 + \alpha_0\left(e_M^2 + e_L^2\right)\right)^{\frac{1}{2}}$ and an effective stress as $t = \left(t_N^2 + \frac{t_M^2 + t_L^2}{\alpha_0}\right)^{\frac{1}{2}}$ are defined on each facet, with $t_N = t\left(\frac{e_N}{e}\right)$, $t_M = \alpha_0 t\left(\frac{e_M}{e}\right)$, $t_L = \alpha_0 t\left(\frac{e_L}{e}\right)$. The magnitude of the effective stress t is limited by a strain-dependent boundary condition $0 \le t \le \sigma_{bt}(e, \omega_{sn})$. $\sigma_{bt}(e, \omega_{sn})$ is described in Eq. (3):

$$\sigma_{bt}(e, \omega_{sn}) = \sigma_0(\omega_{sn}).\exp\left[-H_0(\omega_{sn})\frac{\langle e_{\max} - e_0(\omega_{sn})\rangle}{\sigma_0(\omega_{sn})}\right] \tag{3}$$

with $\langle x \rangle = \max(x, 0)$. ω_{sn} is a variable defining the level of interaction between shear and normal loadings:

$$\tan(\omega_{sn}) = \frac{e_N}{\sqrt{\alpha_0} e_T} = \frac{t_N \sqrt{\alpha_0}}{t_T} \tag{4}$$

e_T is the total shear strain $e_T = \left(e_M^2 + e_L^2\right)^{\frac{1}{2}}$, t_T is the total shear stress $t_T = \left(t_M^2 + t_L^2\right)^{\frac{1}{2}}$, and the maximum effective strain is $e_{\max}(\tau) = \left(e_{N,\max}^2(\tau) + \alpha_0 e_{T,\max}^2(\tau)\right)^{\frac{1}{2}}$ where $e_{N,\max}(\tau) = \max_{\tau' < \tau}\left[e_N(\tau')\right]$ and $e_{T,\max}(\tau) = \max_{\tau' < \tau}\left[e_T(\tau')\right]$.

The strength limit of the effective stress, which defines the transition between pure tension and pure shear, is provided in Eq. (5) where $r_{st} = \sigma_s/\sigma_t$ is the ratio of the shear strength to the tensile strength, σ_s is the shear strength, and σ_t is the tensile strength.

$$\sigma_0(\omega_{sn}) = \sigma_t \frac{-\sin(\omega_{sn})}{2\alpha_0 \cos^2(\omega_{sn})/r_{st}^2} + \sigma_t \frac{\left(\sin^2(\omega_{sn}) + 4\alpha_0 \cos^2(\omega_{sn})/r_{st}^2\right)^{\frac{1}{2}}}{2\alpha_0 \cos^2(\omega_{sn})/r_{st}^2}, \tag{5}$$

The post-peak softening modulus is controlled by the effective softening modulus in Eq. (3), $H_0(\omega_{sn}) = \frac{H_s}{\alpha_0} + \left(H_t - \frac{H_s}{\alpha_0}\right)\left(\frac{2\omega_{sn}}{\pi}\right)^{n_t}$ where $H_t = \frac{2E_0}{l_t/l - 1}$, $H_s = r_s E_0$, and n_t is the softening exponent. Typically, the values of $n_t = 0.2$ and $r_s = 0$ are assumed and fixed. The tensile characteristic length is defined as $l_t = \frac{2E_0 G_t}{\sigma_t^2}$ where G_t is the mesoscale fracture energy.

2.2. Coarse graining

LDPM yields a mesoscale discrete displacement field in a heterogeneous material. Displacements are computed at the centers of particles and stresses are computed on the facets of cells containing a particle. Such quantities will be used for calibration purposes at the macroscale level where the material is considered homogeneous, which is the reason why an intermediate step is implemented, involving a coarse graining method as an upscaling technique yielding continuous macroscale quantities (i.e., stresses, strains, and displacements) from mesoscale discrete LDPM results (Goldhirsch and Goldenberg, 2002; Eid et al., 2021).

First, the upscaled mass density is calculated using a standard convolution product (weighted averaging) in Eq. (6) where R is the mass density of the homogeneous material, ρ is the mass density at mesoscale (heterogeneous) level, ϕ is the convolution function described in Eq. (7), Ω is the domain of interest and $(x)_\phi$ denotes the convolution of x. In this work, the convolution function is a normalized Gaussian function with a coarse graining length denoted as L_{CG}.

$$R(\mathbf{x}) = \rho(\mathbf{x})_\phi = \frac{\int_\Omega \rho(s)\phi(\mathbf{x}, \mathbf{s}) ds}{\int_\Omega \phi(\mathbf{x}, \mathbf{s}) ds} \tag{6}$$

$$\phi(\mathbf{x}, \mathbf{s}) = \frac{1}{\frac{L_{CG}}{3}\sqrt{2\pi}} \exp\left\{\frac{-\|\mathbf{x} - \mathbf{s}\|^2}{2\left(\frac{L_{CG}}{3}\right)^2}\right\} \tag{7}$$

Then, the mass balance equations at the macroscale (9) and at the mesoscale (8) are considered, where $\nabla \cdot (\mathbf{x})$ is the divergence of vector $\mathbf{x}$, $\mathbf{v}$ is the velocity field at the mesoscale, $\mathbf{V}$ is the velocity field at macroscale and $R \cdot \mathbf{V}$ the impulsion.

$$\frac{\partial \rho}{\partial t} + \nabla \cdot (\rho \mathbf{v}) = 0 \tag{8}$$

$$\frac{\partial R}{\partial t} + \nabla \cdot (R \cdot \mathbf{V}) = 0 \tag{9}$$

Upon taking the convolution of the mass balance equation at the mesoscale (8) and comparing with the mass balance equation at the macroscale, one obtains the coarse-grained macroscale velocity as a function of the mesoscale velocity field $\mathbf{v}$, the local mass density ρ and the domain's coarse grained mass density R:

$$\mathbf{V} = \frac{(\rho \mathbf{v})_\phi}{R} \tag{10}$$

For the computation of the macroscale velocity, the mesoscale velocities are assumed to be constant over each cell (see Fig. 1) and the mesoscale mass densities are known (that of aggregate particles and that of cement mortar in between). Applying the convolution product yields macroscale quantities that are continuous in space, whereas mesoscale quantities are not. Further, macroscale displacements are obtained by integrating over time.

The same procedure is applied for the balance of linear momentum. Eqs. (11) and (12) represent momentum conservation at the meso and macroscales respectively, where $\underline{\underline{\sigma}}$ denotes the mesoscale stress tensor and $\underline{\underline{S}}$ represents the macroscale (or coarse-grained) stress tensor.

$$\frac{\partial \rho \mathbf{v}}{\partial t} + \nabla \cdot (\rho \mathbf{v} \otimes \mathbf{v}) = \nabla . (\underline{\underline{\sigma}}) \tag{11}$$

$$\frac{\partial R \mathbf{V}}{\partial t} + \nabla \cdot (R \mathbf{V} \otimes \mathbf{V}) = \nabla . (\underline{\underline{S}}) \tag{12}$$

Upon taking the convolution of Eq. (11) and using Eq. (10), the following relationship is obtained:

$$\frac{\partial R \mathbf{V}}{\partial t} = \frac{\partial (\rho \mathbf{v})_\phi}{\partial t} = (\nabla \cdot (\underline{\underline{\sigma}}) - \nabla \cdot (\rho \mathbf{v} \otimes \mathbf{v}))_\phi \tag{13}$$

Introducing the fluctuating velocity $\mathbf{v}' = \mathbf{v} - \mathbf{V}$ and inserting it in Eq. (13) yields:

$$\frac{\partial R \mathbf{V}}{\partial t} + \nabla \cdot (R \cdot \mathbf{V} \otimes \mathbf{V}) = (\nabla \cdot (\underline{\underline{\sigma}}) - \nabla \cdot (\rho \mathbf{v}' \otimes \mathbf{v}'))_\phi \tag{14}$$

The conservation of momentum at the macroscale (Eq. (12)) may now be used to obtain Eq. (15) relating the coarse grained stress $\underline{\underline{S}}$ to the mesoscale stress ($\underline{\underline{\sigma}}$), mass density ($\rho$), and fluctuation velocity ($\mathbf{v}'$):

$$\underline{\underline{S}} = (\underline{\underline{\sigma}} - (\rho \mathbf{v}' \otimes \mathbf{v}'))_\phi \tag{15}$$

In quasi-static computations, the effect of fluctuating velocity is usually neglected (see e.g. Eid et al., 2021) and we shall use the same assumption which simplifies Eq. (15) to $\underline{\underline{S}} = (\underline{\underline{\sigma}})_\phi$.

Coarse grained displacements are obtained at the nodes of an arbitrary fine grid used for computing the convolution product. This grid may also serve as a finite element mesh with shape functions, so that strains may be derived accordingly. Upon coarse graining, it is important that stresses and strains are computed at the same points, i.e. at the gauss points of the mesh used for computing the displacements. It means that the grid used for computing stresses corresponds to the gauss points of the finite element mesh used for computing displacements.

In addition, LDPM yields stress vectors at the facets. These vectors are converted into a tensor which is computed at the center of each grain and constant over the cell. It is the second-order mesoscale stress tensors required as an input in Eq. (15). For this purpose, several approaches can be found in the literature. Among the most well-known is the Love–Weber formula, which involves computing the tensor product of the contact force between particles and the vector joining the centers of the grains (Nicot et al., 2013; Wan et al., 2015). Here, the facet stresses t_k from every polyhedral cell are gathered and used to estimate the stress tensor $\underline{\underline{\sigma}}$ at the center of each particle. This is done by solving the following weak-form equation:

$$\text{Find } \underline{\underline{\sigma}} \text{ such that } \sum_k \left[\left(\underline{\underline{\sigma}} \cdot \hat{\mathbf{n}}_k - \mathbf{t}_k\right) \cdot \left(\underline{\underline{\varepsilon}}^* \cdot \hat{\mathbf{n}}_k\right)\right] = 0, \quad \forall \underline{\underline{\varepsilon}}^* \tag{16}$$

where $\hat{\mathbf{n}}_k$ is the unit normal vector to facet k, t_k is the corresponding facet stress, and $\boldsymbol{\varepsilon}^*$ is a virtual strain tensor. Assuming isotropic behavior, the number of unknowns in the stress tensor is reduced to six. Accordingly, six virtual strain tensors are considered: three uniaxial strain tensors and three pure shear strain tensors, leading to a system

of six equations that can be solved to determine the six unknown stress components.

Finally, note that the macroscopic displacements and stresses are calculated separately by coarse graining the balance equations. There is no a priori assumption on the mechanical response at the macroscale, which is simply the result of upscaling separately kinematic and static quantities.

2.3. Macroscale CDM model

The macroscale model is a nonlocal isotropic damage model (Pijaudier-Cabot and Bažant, 1987). The stress vs. strain relationship is defined in Eq. (17) where $\underline{\underline{S}}$ is the second order (macroscale) stress tensor, $\underline{\underline{\varepsilon}}$ is the second order macroscale strain tensor, $\mathbb{C}$ is the fourth order elastic stiffness tensor, and D the damage scalar.

$$\underline{\underline{S}} = (1 - D) \cdot \mathbb{C} : \underline{\underline{\varepsilon}} \tag{17}$$

Damage growth is controlled by the nonlocal equivalent strain $\bar{\varepsilon}$:

$$\bar{\varepsilon}(\mathbf{x}) = \frac{\int \psi(\mathbf{x}, \mathbf{s}) \tilde{\varepsilon}(\mathbf{s}) dv}{\int \psi(\mathbf{x}, \mathbf{s}) dv} \tag{18}$$

where ψ is a Gaussian function with an internal length denoted by L_C, and $\tilde{\varepsilon}$ is the local equivalent strain, function of the positive part of the principal strains:

$$\tilde{\varepsilon} = \sqrt{\sum_{i=1}^{3} (\langle \varepsilon_i \rangle_+)^2} \tag{19}$$

where $\langle x \rangle_+$ is the Macaulay bracket and ε_i is the principal strain component. The limit of the reversible behavior is defined in Eq. (20) (Mazars, 1986).

$$\mathbb{K}(x, t) = max_{[0,t]} \left(\bar{\varepsilon}(x, t) \ , \ K_{tr0} \right) \tag{20}$$

$\mathbb{K}$ is a history parameter that keeps records of previously triggered damage, and K_{tr0} is the threshold of the damage. If $d\varepsilon \leq 0$ and $f(\bar{\varepsilon}) = 0$ or $f(\bar{\varepsilon}) < 0$, damage will not occur. Damage growth results from high tensile strains, such as when $f(\bar{\varepsilon}) = 0$ and $d\varepsilon > 0$. Eq. (21) describes the damage in this model:

$$g(\mathbb{K}) = \alpha_t \cdot D_t + \alpha_c \cdot D_c \tag{21}$$

$D_{t,c}$ and $\sigma^{t,c}$ are the tensile and compressive damage parameters and stresses respectively (for more details, see Mazars and Pijaudier-Cabot 1989). The damage evolution laws are given in Eq. (22). $A_{t,c}$ and $B_{t,c}$ are model parameters.

$$D_{t,c} = 1 - \frac{K_{tr0}(1 - A_{t,c})}{\mathbb{K}} - \frac{A_{t,c}}{\exp^{B_{t,c}(\mathbb{K} - K_{tr0})}} \tag{22}$$

2.4. Calibration

The specimen geometry and boundary condition for the calibration corresponds to one of the specimen sizes considered in the experimental study of size effect by Grégoire et al. (2013), the next to smallest with a notch length $a = 0.2$ times the beam depth. A micro-concrete was considered and the distribution of aggregates, needed for the definition of LDPM specimens was also provided.

Five three-point bending LDPM calculations were performed on five distinct samples, each with a unique discrete or aggregate distribution. Grains in one of the LDPM samples are shown in Fig. 2, while LDPM parameters, geometry, and loading conditions are kept constant across all calculations. The important LDPM characteristics are summarized in Table 1.

Fig. 3 shows the force–displacement responses for the five LDPM calculations.

Coarse graining was performed over the entire load–deflection history. A regular finite element mesh with linear interpolation of the displacements is superimposed on the LDPM mesh. Displacements are upscaled first on the finite element nodes using the mesoscale LDPM displacements located at the center of each LDPM particle. Strains are then computed at each Gauss point. Stresses are directly upscaled at the same Gauss points. This upscaling process yields stress fields vs. strain field histories over the specimen. In Khoury et al. (2026), the coarse graining length was determined separately, by allowing a correlation length on the fluctuations of stresses less than 1 percent in the elastic regime and for a tensile test on a cylindrical rod. The obtained coarse graining length for this material was $L_{C,G} = 4D_{max}$. Then, calibration was performed: (1) the history variable was derived from the local stress field histories at every discrete point (on a regular grid) located in a window centered at the notch of width equal to twice the maximum aggregate size; (2) given the history variable, the damage parameter was computed according to the stress–strain history at the same discrete points, where strains and stresses are provided also. In doing so, the evolution law for damage which relates the history variable to damage at the macroscale was constructed at each discrete material point, over the window, and the results were gathered into a single curve; (3) Eq. (22) was fitted and the material parameters A_t, B_t, and the damage threshold K_{tr0} were obtained; (4) the process was repeated for various values of the internal length L_c and the optimal set which yielded the least calibration error with respect to the evolution of damage was selected. Note that elastic constants are not included in this procedure. They are assumed to be obtained from calibration in the elastic regime prior to considering nonlinear responses.

Table 1
LDPM model parameters.

Normal Modulus	E_0	43,195 MPa
Alpha	α	0.25
Tensile Strength	σ_t	4.6 MPa
Tensile Characteristic Strength	l_t	200 mm
Shear Strength ratio	r_t	2.5

Table 2
Nonlocal damage model parameters.

L_C	A_t	B_t	K_{tr0}
low $4D_{max}$	0.9	3708	$4.09e^{-5}$
average $4D_{max}$	0.83	3635	$2.43e^{-5}$
high $4D_{max}$	0.67	3503	$9.92e^{-6}$

Given the LDPM parameters listed in Table 1, optimization yielded the model parameters for the nonlocal damage model listed in Table 2. Three sets have been obtained. The one labeled as "average" denotes the optimal set, the ones labeled as "low" or "high" denote respectively the best set of model parameters corresponding to the lower bound and upper bound envelopes of the damage evolution law.

Using these optimal parameters, the comparison of global responses obtained from LDPM and CDM was found to be quite satisfactory. Results from Khoury et al.'s work 2026 are shown in Fig. 4. However, in quasi-brittle materials such as concrete, structural size effect is observed. Capturing this phenomenon is among the distinctive results that a proper model for concrete should provide Bažant and Nguyen (2023). As we will see next, the above calibration turns out to yield an incorrect size effect, meaning that the FPZ is not captured properly.

3. Prediction of size effect and constrained calibration

It has been demonstrated that both the macroscale CDM model and the mesoscale LDPM model provide a consistent prediction of size effect on notched bending beams (Pathirage et al., 2023; Le Bellégo et al., 2003). Therefore, the comparison between the predictions of size effect

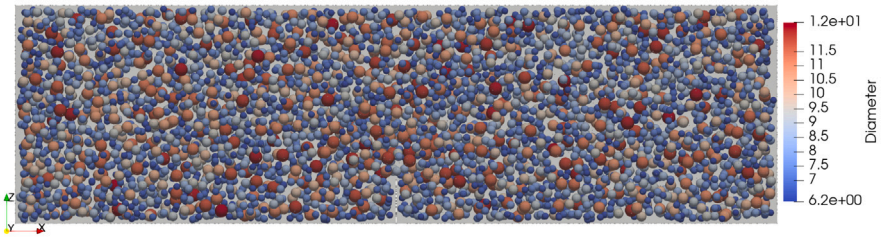

Fig. 2. LDPM grains in one of the notched beam samples.

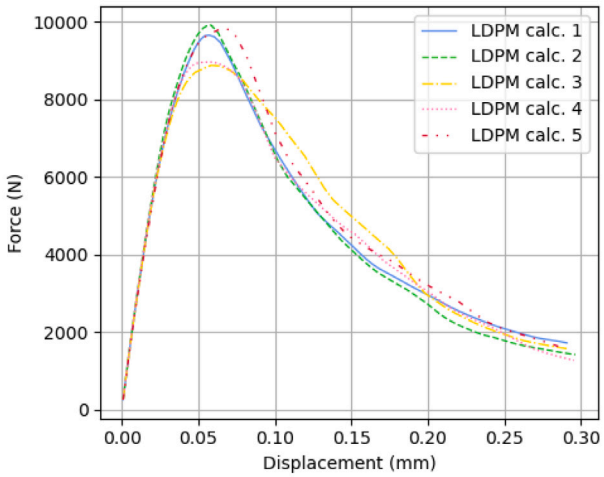

Fig. 3. Load versus displacement responses for 5 LDPM calculations.

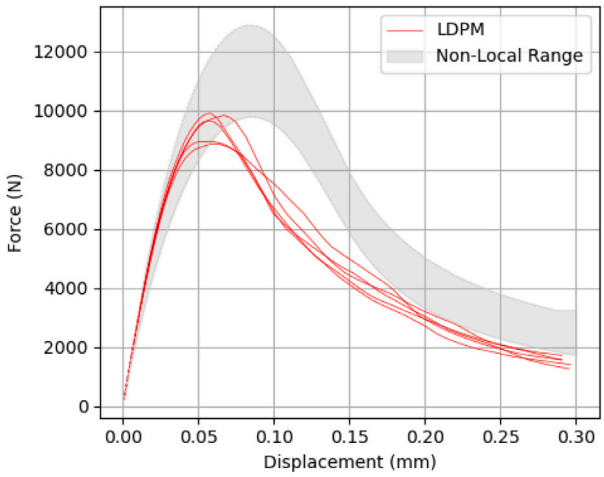

Fig. 4. Comparison of the predicted global response from the calibrated CDM with the LDPM responses (after Khoury et al., 2026).

according to LDPM and CDM, with the model parameters provided in the previous section, should shed light on the quality of the above calibration process.

Size effect calculations have been performed for three geometrically identical beams with different sizes and a fixed thickness (50 mm). Fig. 5 shows all sizes, while larger beams are displayed in light gray in each figure. The beam depths are 100 mm, 200 mm, and 400 mm, with a span-to-depth ratio of 2.5. The notch is 2 mm thick with a length-to-depth ratio of 1/5. Recall that for calibration, only the beam depth of 100 mm was considered.

Bažant's size effect theory is used for the interpretation of the results, meaning that peak loads are considered only Bažant and Planas (2019). Size effect is expressed as the relationship between the characteristic dimension, D, and the nominal stress, σ_N. Simple beam formula $\sigma_N = \frac{3}{2}\frac{FL}{b(0.8D)^2}$ is used for the calculation of the nominal stress. F is the maximum load, L is the span, b is the beam's width, and D is the depth of the beam. Eq. (23) shows the size effect formula:

$$\sigma_N = \frac{Bf_t}{\sqrt{1+\frac{D}{D_0}}} \tag{23}$$

where B is a parameter function of the geometry and load system applied to the sample, f_t is the tensile strength, D the sample dimension, and D_0 a characteristic dimension. Through linear regression in the form $Y = AX + C$, where $X = D$, $Y = (\frac{1}{\sigma_N})^2$, $Bf_t = \frac{1}{\sqrt{C}}$, and $D_0 = \frac{C}{A}$, the values of Bf_t and D_0 are obtained.

In the present case, the LDPM response is the reference and the size effect parameters were fitted from LDPM calculations of the peakload. Then, CDM (plane stress) calculations have been performed. Fig. 6 shows the size effect calculation results where $log\left(\frac{\sigma_N}{Bf_t}\right)$ is plotted versus $log\left(\frac{D}{D_0}\right)$.

Error bars on the macroscale calculations show the expected range of peak loads depending on the set of model parameters considered in Table 2. Despite an optimal set of macroscale model parameters has been obtained from the calibration on beams of a given size, size effect is not well predicted by the macroscale CDM model. Peak loads are overestimated, and most importantly this overestimation depends on the specimen size: it decreases as the specimen size increases. It means that the width of the FPZ, which depends on the internal length is not properly captured (recall that such structural size effect originates from the variation of the ratio of the width of the FPZ – a constant – to the size of the beam).

To get some insight on the discrepancy observed between LDPM and CDM results, it is interesting to focus on the energy dissipation within the FPZ. At each material point, the density of energy dissipated W_d (dissipation per unit volume) is the integral of the constitutive response minus the reversible (elastic energy).

$$W_d(\mathbf{x}) = \int_0^{\max(\underline{\underline{\varepsilon}})} \underline{\underline{S}}(\mathbf{x}) : d\underline{\underline{\varepsilon}}(\mathbf{x}) - \frac{(1-D(\mathbf{x}))}{2} \max(\underline{\underline{\varepsilon}}(\mathbf{x})) : \mathbb{C} \cdot \max(\underline{\underline{\varepsilon}}(\mathbf{x})) \tag{24}$$

where $\max(\underline{\underline{\varepsilon}}(\mathbf{x}))$ is the strain tensor over the loading history which yielded the current value of damage at point $\mathbf{x}$. To obtain the total dissipated energy, integration over the volume of the finite element mesh/particle cell is performed in LDPM calculations. After coarse graining and for the nonlocal damage calculations, we have computed the energy dissipation per unit volume only and scaled them to fit the peak of dissipation obtained in LDPM calculations. This procedure enabled a comparison of LDPM, coarse grained and nonlocal damage calculations.

Fig. 7(b) compares the energy dissipated along an horizontal line at midspan according to the LDPM calculation, to the coarse grained results, and finally to the nonlocal damage model. This plot has been extracted at a loading stage located in the softening regime of the load — deflection curve (see Fig. 7(a)). The agreement between the width

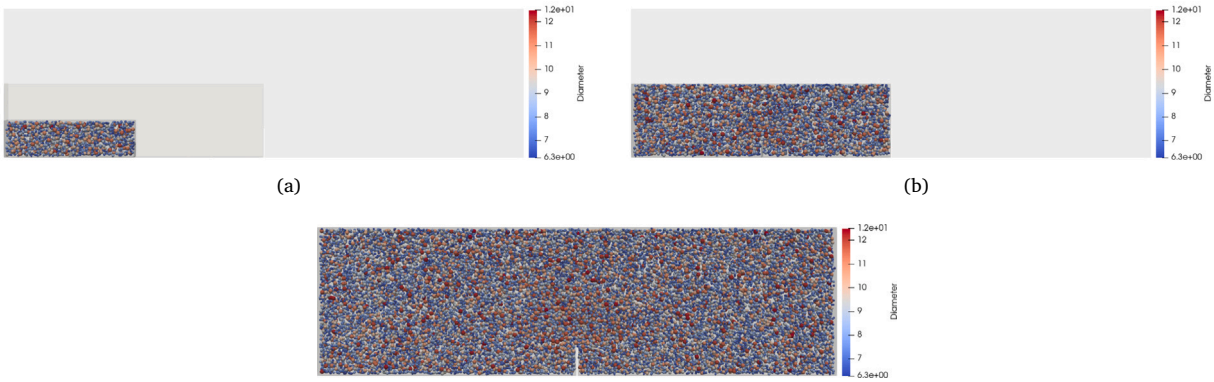

Fig. 5. Geometrically similar beams for size effect calculations. Depths are (a) 100 mm, (b) 200 mm and (c) 400 mm.

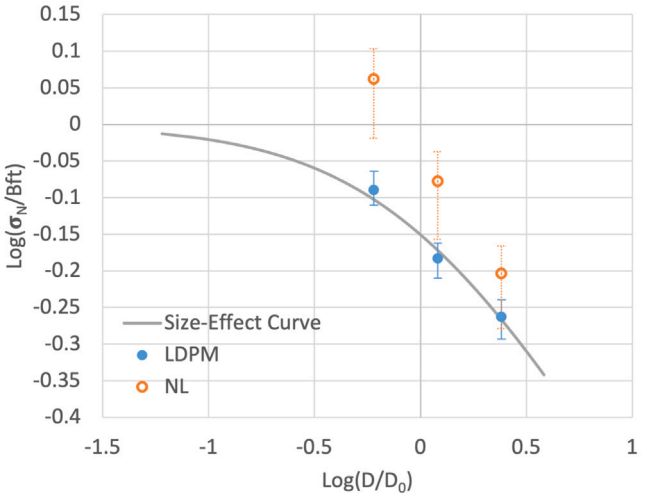

Fig. 6. Size effect calculation: comparison of LDPM and CDM results calibrated from Khoury et al. (2026).

obtained by the coarse grained LDPM results and the macroscale results demonstrate that indeed, the calibration process yielded a correct description of the FPZ, as predicted by the coarse grained results. This fit, however does not correspond to LDPM results without coarse graining.

Fig. 8 shows the distribution of energy dissipation over the beam according to LDPM at the same load level in the softening regime.

It can be observed that the FPZ spans over 2 to 3 maximum aggregate sizes, which is much lower than what CDM predicts. Because the FPZ width is overestimated in the CDM calculation compared to the LDPM calculation, predictions of size effect cannot coincide. A direct consequence is that the fracture energy in the CDM model, measured with the size effect test method, is different from that obtained for the LDPM calculation, meant to be the reference.

Since the internal length L_C is directly related to the width of the FPZ, and since the CDM model should provide a description of the width of the FPZ consistent with the reference (LDPM) calculations, it appears preferable to choose an internal length that yield the correct width of the FPZ.

Fig. 9 shows the dissipated energy for the LDPM and three different nonlocal calculations with internal lengths ranging from one to three times the maximum aggregate size. Setting the internal length in the nonlocal model as twice the maximum aggregate size ($L_C = 2D_{max}$) provides a width of the FPZ in the nonlocal model close to that observed in the LDPM calculation. Therefore, the calibration of the nonlocal

Table 3
SSR variation with the variation of L_{CG}.

L_C	L_{CG}	SSR
$2D_{max}$	$1D_{max}$	1.468e−01
$2D_{max}$	$2D_{max}$	3.889e−02
$2D_{max}$	$3D_{max}$	3.577e−02
$2D_{max}$	$4D_{max}$	2.381e−02
$2D_{max}$	$5D_{max}$	2.941e−02

model is performed again with a fixed internal length $L_C = 2D_{max}$. The coarse graining length is no longer fixed now, but belongs to the parameters that may change in the course of optimization, in case both lengths might interact.

The calibration process is the same as described in the previous chapter, except that several values of the coarse graining length are considered while keeping the internal length fixed. A variable coarse graining length that ranged from one to five times the maximum aggregate size has been considered. The nonlocal damage model has been calibrated using the reconstructed relationship between D and $\mathbb{K}$ for each coarse grained length. The difference between the D and $\mathbb{K}$ values derived from the fitted nonlocal model and the coarse-grained data has also been measured using the Sum of Squared Residuals (SSR) and results are shown in Table 3. The optimal fit of the nonlocal model is defined by the minimum value of the SSR. It turns out that the coarse graining length that minimizes the SSR is $L_{CG} = 4D_{max}$. Given that the coarse graining length has been varied with a resolution of D_{max}, it is greater than $3D_{max}$ and lower than $5D_{max}$. In fact, we have recovered the same value of the coarse graining length as the one used in Khoury et al. (2026), although it was derived from the analysis of stress fluctuations. This result shows that the two lengths do not seem to interact.

Fig. 10 shows the D vs. $\mathbb{K}$ plot from CG-LDPM points as well as for the calibrated nonlocal models. The upper and lower bounds of the D–$\mathbb{K}$ plot are taken into consideration to capture all potential solutions. Three sets of nonlocal parameters are identified again: one for the best match and two for the upper and lower bounds as shown in Fig. 10. Compared to the value provided in Table 2 there is a slight change of the model parameters.

Fig. 11 shows the force–displacement results from the five LDPM calculations alongside the nonlocal model results. With the exception of a few points in the post-peak curve, where the LDPM forces slightly exceed those from the nonlocal model, CDM results are now in very good agreement with the reference LDPM results. This agreement is better than the one observed by considering the coarse graining length fixed and letting the internal length free. Both fitting techniques lead approximately to the same value of the coarse graining length which

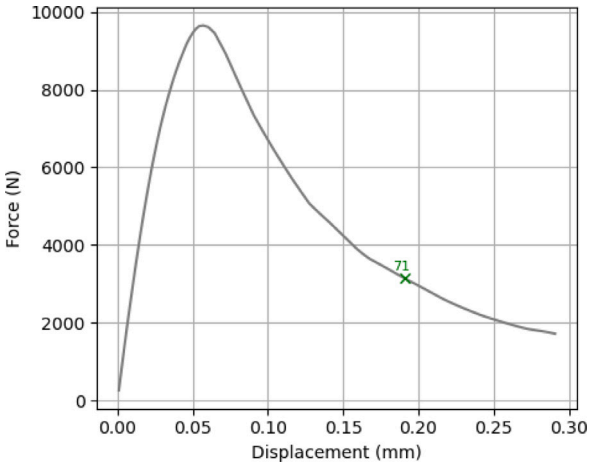

(a) Calculation step 71 in one of the LDPM calculations.

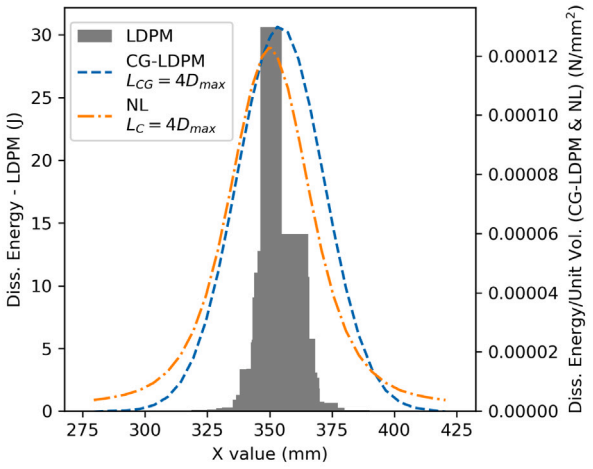

(b) Dissipated energy in LDPM, CG-LDPM and NL calculation in Khoury et al. (2026) at calculation step 71.

Fig. 7. Comparison of energy dissipation according to LDPM and to the nonlocal model.

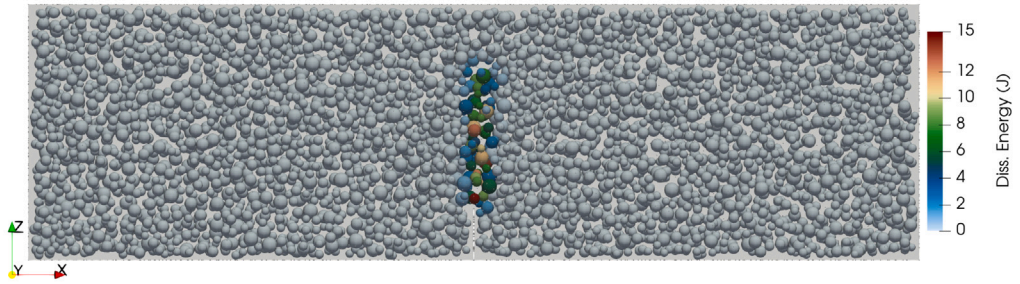

Fig. 8. Map of dissipated energy according to LDPM at calculation step 71 in J mm.

shows that calibration of the coarse graining length can be performed in the elastic regime only. Overall, constraining the model to capture accurately the width of the FPZ by setting $L_C = 2D_{max}$ provides a much more accurate description of the global response.

Fig. 12 shows the energy dissipation curves from an LDPM calculation, alongside those from the current nonlocal model, calibrated using $L_{CG} = 4D_{max}$ and $L_C = 2D_{max}$, and from the nonlocal model with $L_{CG} = 4D_{max}$ and $L_C = 4D_{max}$. With the present calibration, the computation captures well the width of the fracture process zone (FPZ) observed in the LDPM calculation.

Further, size effect calculations on notched bending beams can be performed again with the CDM model and the new set of material parameters. Results are shown in Fig. 13.

We observe that a consistent description of the FPZ, here the width of the FPZ, is the important feature if one wants to extrapolate results on specimens of various sizes.

4. Comparison on a different geometry

Let us now compare LDPM results with the calculations performed with the calibrated nonlocal damage model on a different geometry. The aim is to check that the macroscale continuum damage prediction does not yield large error upon predicting the response of specimens with a geometry that is different from that used for calibration.

An L-shaped specimen with a height of 400 mm and a depth of 50 mm is considered. The specimen is made of the same material and uses the same LDPM parameters. The specimen, illustrated in Fig. 14(a), is fixed along its bottom face and subjected to a vertical load applied from the side. The force–displacement results are shown in Fig. 14(b). Calculations have been performed for three different LDPM meshes and also for the three sets of parameters in the CDM model, defining its range of predictions.

CDM computations do not exactly match with LDPM results. This mismatch is not due to a misfit on the elastic response but it results from a relatively poor prediction of the onset of nonlinear behavior. In the nonlocal model, the nonlinear behavior initiates earlier than in the LDPM results. The K_{tr0} parameter, which is the threshold of inception of damage is the cause of this discrepancy. This threshold, which significantly impacts the calculations, exhibits the largest variation in the fits after considering the extreme possibilities shown in Fig. 10. It is this one which is obtained with less accuracy in the present calibration procedure.

Size effect on L-shaped samples has also been considered. The peak loads computed for specimens with heights of 200 mm, 400 mm, 800 mm, and 1600 mm, and a constant depth of 50 mm have been obtained from LDPM and nonlocal damage computations. The samples are shown in Fig. 15. The size effect plot, following Bažant's size effect equation, is shown in Fig. 16.

The nominal stresses obtained from LDPM calculations are slightly higher than those predicted by the nonlocal model. Most importantly, there is a constant (in a log–log plot) downward shift of the nonlocal results compared to the LDPM results. This downward shift may be interpreted as the result of the underestimation of the peakload observed for one specimen size in Fig. 14(b). Again, a relatively inaccurate determination of the damage threshold yields a loss of accuracy in the prediction of the peakload. However, the trend on the variation of the nominal stress of the specimen with the specimen size is still rather well depicted, as a result of a better description of the size of the FPZ.

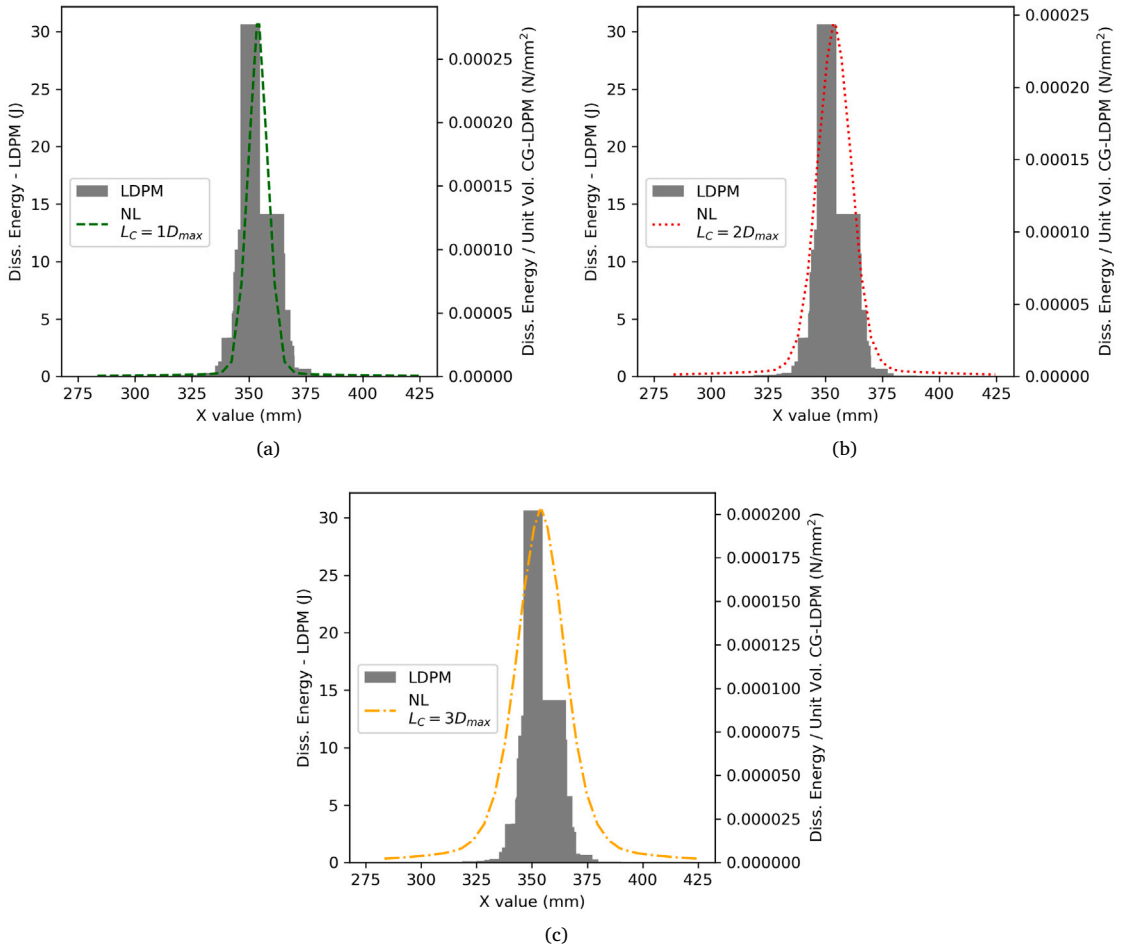

Fig. 9. The dissipated energy from LDPM and nonlocal calculation with (a) $L_C = 1D_{max}$, (b) $L_C = 2D_{max}$ and (c) $L_C = 3D_{max}$.

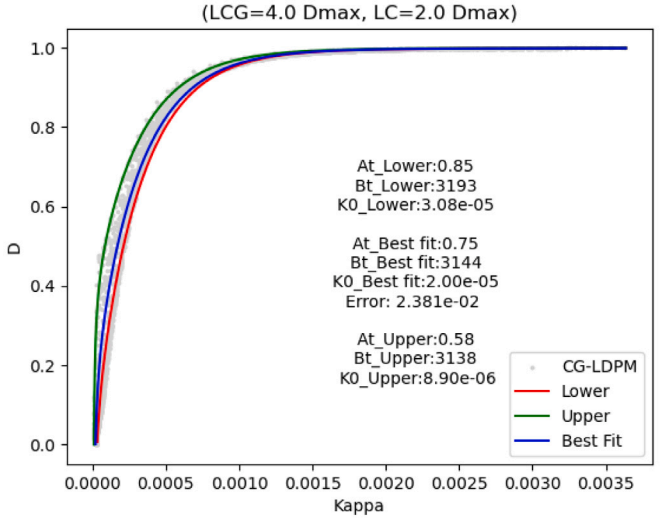

Fig. 10. D vs. $\mathbb{K}$ plot for $L_{CG} = 4D_{max}$ and $L_C = 2D_{max}$ as well as the three nonlocal models. The model parameters in the damage evolution law and their range of variation is also provided.

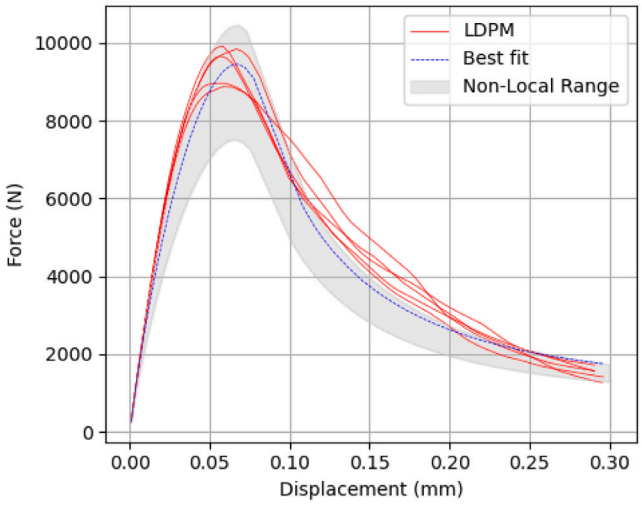

Fig. 11. Comparison between LDPM load–deflection curves and the range of curves obtained according to the calibrated nonlocal model.

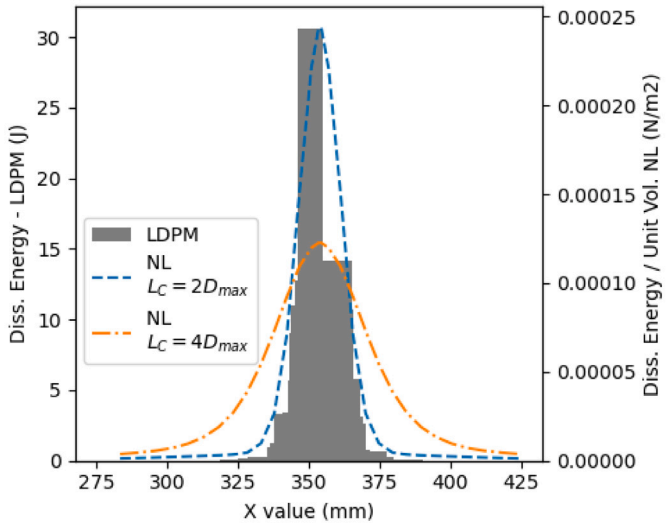

Fig. 12. Dissipated energy from LDPM and the two nonlocal calculations with $L_C = 2_D max$ and $L_C = 4_D max$ according to the unconstrained and constrained calibrations.

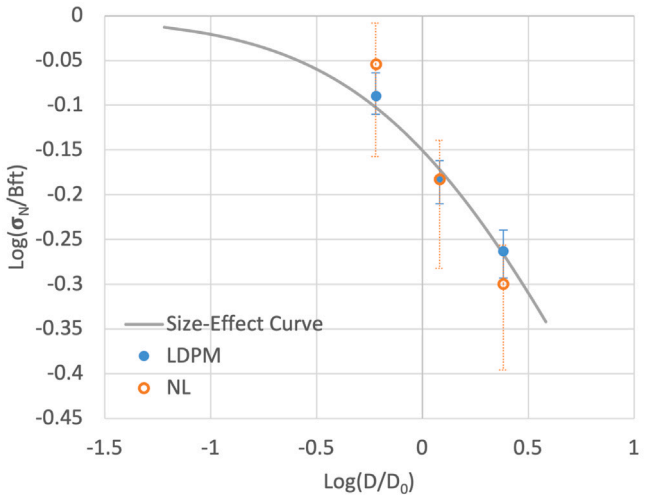

Fig. 13. Size effect prediction according to the nonlocal model with a constrained calibration.

5. Conclusion

Nonlocal models for fracture can be calibrated from field data, e.g., strain fields, stress and other internal variable fields, including their internal length. There is no need to consider specimens of various geometries or size effect data because the correlation upon failure that is induced by the nonlocal model is included in field data.

This paper started from an initial study where calibration was considered using LDPM viewed as a high-fidelity model. The calibration procedure mainly involved two lengths: the coarse graining length, which is related to the size of the RVE in the reversible regime, and the nonlocal damage model length, which is related to width of the FPZ. In the initial study, the coarse graining length was determined by minimizing stress fluctuations in the elastic response of an uniaxially loaded specimen, and then the internal length, along with the model parameters entering in the evolution of damage, were obtained. We show here that such a procedure yields a poor description of size effect, due to an overestimated width of the FPZ.

A proper calibration needs to start from an accurate description of the size of the FPZ. The present study shows that it is much better to constrain the internal length in the nonlocal model to fit the width of the FPZ prior to calibration. The evolution law of damage is fitted for several different values of the coarse graining length, and the residual error is computed. The fit with the lowest residual error is considered as the best calibration. This yields a coarse graining length which turns out to be the same as the one obtained in the initial study (Khoury et al., 2026), meaning that the two lengths do not seem to interact.

Calibration leads to a range of model parameters corresponding to the mean, lower bound envelope, and upper bound envelope of the cloud of points obtained from mesoscale results. Load–deflection responses computed according to this range of model parameters agree with the LDPM structural responses. More importantly, size effect is predicted consistently because the FPZ is best captured.

Comparison with an L-shaped specimen response shows that, after calibration on notched bending beams, there are still some residual errors. Results lie within the same order of magnitude as the LDPM calculations but underestimate the peak load. This difference is due to an underestimation of the tensile strength, related to the onset of nonlinear response, which is difficult to fit with high accuracy. It should be underlined that the damage model used for this study remains quite simplistic. It may be among the reasons why predictions on different geometries do not match exactly.

As a closing comment, and following the methodology used when coarse graining is performed, energy balance could be also coarse-grained. If the field of dissipated energy is extracted, that may yield potentially another way to constrain the size of the FPZ and reach a similar objective. In this case the internal length would result from the calibration instead of being fixed separately from the dissipation profiles. Such a direction needs, however, to be examined in more details.

CRediT authorship contribution statement

Julien Khoury: Writing – original draft, Investigation, Formal analysis. **Gilles Pijaudier-Cabot:** Writing – review & editing, Methodology, Funding acquisition, Formal analysis, Conceptualization. **Gianluca Cusatis:** Writing – review & editing, Supervision, Methodology, Investigation, Conceptualization.

Declaration of competing interest

The authors declare the following financial interests/personal relationships which may be considered as potential competing interests: Gilles Pijaudier-Cabot reports financial support was provided by French National Research Agency. Julien Khoury reports financial support was provided by European Union. If there are other authors, they declare that they have no known competing financial interests or personal relationships that could have appeared to influence the work reported in this paper.

Acknowledgments

Partial financial support from the investissement d'avenir French programme (ANR-16-IDEX- 0002), the European Union's Horizon 2020 research and innovation programme EDENE under the Marie Skłodowska-Curie grant agreement No 945416, and from the Communauté d'Agglomération Pau – Béarn – Pyrennées are gratefully acknowledged. This research was performed in part within the E2S hub Newpores supported jointly by Université de Pau et des Pays de l'Adour and Northwestern University.

Data availability

Data will be made available on request.

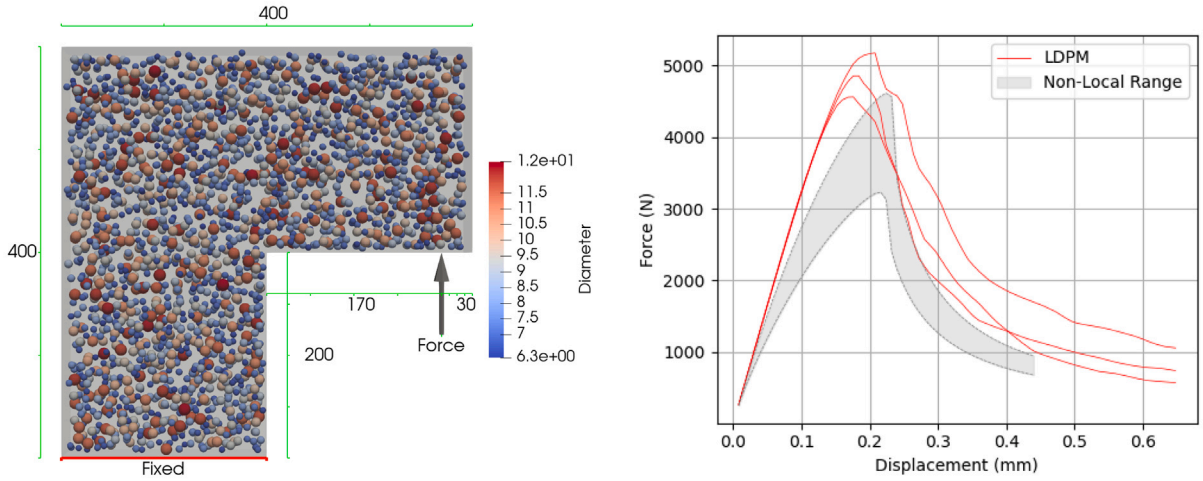

(a) L-Shaped specimen Geometry.

(b) L-Shaped specimen calculation results

Fig. 14. L-Shaped Beam.

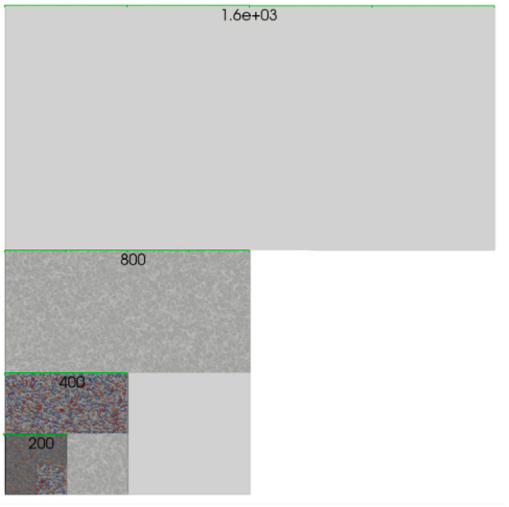

Fig. 15. L-Shaped samples.

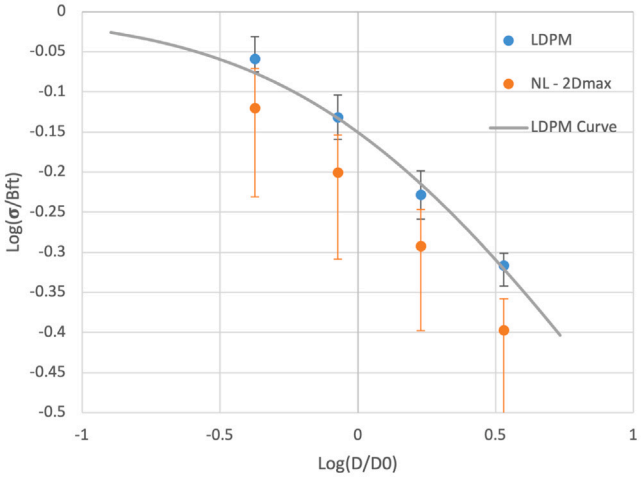

Fig. 16. Size effect calculations for L-Shaped specimens.

References

Arruda, M.R.T., Pacheco, J., Castro, L.M.S., Julio, E., 2022. A modified mazars damage model with energy regularization. Eng. Fract. Mech. 259, 108129.

Bažant, Z.P., Nguyen, H.T., 2023. Proposal of m-index for rating fracture and damage models by their ability to represent a set of distinctive experiments. J. Eng. Mech. 149 (8), 04023047.

Bažant, Z.P., Planas, J., 2019. Fracture and Size Effect in Concrete and Other Quasibrittle Materials. Routledge.

Bolander, J.E., Eliáš, J., Cusatis, G., Nagai, K., 2021. Discrete mechanical models of concrete fracture. Eng. Fract. Mech. 257, 108030.

Cusatis, G., Pelessone, D., Mencarelli, A., 2011. Lattice discrete particle model for failure behavior of concrete. I: Theory. Cem. Concr. Compos. 33 (9), 881–890.

Desmorat, R., Gatuingt, F., Ragueneau, F., 2007. Nonlocal anisotropic damage model and related computational aspects for quasi-brittle materials. Eng. Fract. Mech. 74 (10), 1539–1560.

Eid, E., Seghir, R., Réthoré, J., 2021. Multiscale analysis of brittle failure in heterogeneous materials. J. Mech. Phys. Solids 146, 104204.

Feng, Wu, J.-Y., 2018. Phase-field regularized cohesive zone model (CZM) and size effect of concrete. Eng. Fract. Mech. 197, 66–79.

Geers, M., de Borst, R., Peijs, T., 1999. Mixed numerical-experimental identification of non-local characteristics of random-fibre-reinforced composites. Compos. Sci. Technol. 59 (10), 1569–1578.

Goldhirsch, I., Goldenberg, C., 2002. On the microscopic foundations of elasticity. Eur. Phys. J. E 9, 245–251.

Grégoire, D., Rojas-Solano, L.B., Pijaudier-Cabot, G., 2013. Failure and size effect for notched and unnotched concrete beams. Int. J. Numer. Anal. Methods Geomech. 37 (10), 1434–1452.

Haidar, K., Pijaudier-Cabot, G., Dubé, J.-F., Loukili, A., 2005. Correlation between the internal length, the fracture process zone and size effect in model materials. Mater. Struct. 38, 201–210.

Heinzmann, J., Carrara, P., Luo, C., Manav, M., Mishra, A., Nagajara, S., Oudich, H., Vincentini, F., De Lorenzis, L., 2024. Calibration and validation of a phase-field model of brittle fracture within the damage mechanics challenge. Eng. Fract. Mech. 307, 110319.

Khoury, J., Cusatis, G., Pijaudier-Cabot, G., 2026. Informing a damage model for fracture of concrete from lattice discrete particle model results. Int. J. Damage Mech. http://dx.doi.org/10.1177/10567895261421295.

Kosin, V., Fau, A., Hild, F., Wick, T., 2024. Parameter identification of a phase-field fracture model using integrated digital image correlation. Comput. Methods Appl. Mech. Engrg. 420, 116689.

La Borderie, C., 2003. Stratégies et Modèles de Calculs pour les Structures en Béton. Habilit. à Dir. des Rech. Université de Pau et Des Pays de L'Adour, Fr..

Le Bellégo, C., Dubé, J.F., Pijaudier-Cabot, G., Gérard, B., 2003. Calibration of nonlocal damage model from size effect tests. Eur. J. Mech. A Solids 22 (1), 33–46.

Lyu, U., Pathirage, M., Nguyen, H.T., Bažant, Z.P., Cusatis, G., 2023. Dissipation mechanisms of crack-parallel stress effects on fracture process zone in concrete. J. Mech. Phys. Solids 181, 105439.

Mazars, J., 1986. A description of micro-and macroscale damage of concrete structures. Eng. Fract. Mech. 25 (5–6), 729–737.

Mazars, J., Pijaudier-Cabot, G., 1989. Continuum damage theory—application to concrete. J. Eng. Mech. 115 (2), 345–365.

Miehe, C., Welschinger, F., Hafacker, M., 2010. Thermodynamically consistent phase-field models of fracture: Variational principles and multi-field FE implementations. Internat. J. Numer. Methods Engrg. 83, 1273–1311.

Nicot, F., Hadda, N., Guessasma, M., Fortin, J., Millet, O., 2013. On the definition of the stress tensor in granular media. Int. J. Solids Struct. 50 (14–15), 2508–2517.

Pathirage, M., Tong, D., Thierry, F., Cusatis, G., Grégoire, D., Pijaudier-Cabot, G., 2023. Discrete modeling of concrete failure and size-effect. Theor. Appl. Fract. Mech. 124, 103738.

Peerlings, R.H.J., De Borst, R., Brekelmans, W.A.M., De Vree, J.H.P., 1996. Gradient enhanced damage for quasi-brittle materials. Internat. J. Numer. Methods Engrg. 39 (19), 3391–3403.

Pijaudier-Cabot, G., Bažant, Z.P., 1987. Nonlocal damage theory. J. Eng. Mech. 113 (10), 1512–1533.

Pijaudier-Cabot, G., Toussaint, D., Pathirage, M., Cusatis, G., 2024. The role of the horizon in modeling failure due to strain and damage localization with peridynamics. J. Eng. Mech. - ASCE 150 (7), 04024037.

Rezakhani, R., Scott, D.A., Bousikhane, F., Pathirage, M., Moser, R.D., Green, B.H., Cusatis, G., 2021. Influence of steel fiber size, shape, and strength on the quasi-static properties of ultra-high performance concrete: Experimental investigation and numerical modeling. Constr. Build. Mater. 296, 123532.

Schauffert, E.A., Cusatis, G., 2012. Lattice discrete particle model for fiber-reinforced concrete. I: Theory. J. Eng. Mech. 138 (7), 826–833.

Silling, S.A., Askari, E., 2005. A meshfree method based on the peridynamic model of solid mechanics. Comput. Struct. 83 (17–18), 1526–1535.

Silling, S.A., Epton, M., Weckner, O., Xu, J., Askari, E., 2007. Peridynamic states and constitutive modeling. J. Elasticity 88 (2), 151–184.

Védrine, L., Loiseau, F., Oliver-Leblond, C., Desmorat, R., 2025. Calibration of non-local damage models from full-field measurements: Application to discrete element fields. Eur. J. Mech. A Solids 112, 105611.

Wan, R., Duriez, J., Darve, F., 2015. A tensorial description of stresses in triphasic granular materials with interfaces. Geomech. Energy Environ. 4, 73–87.

Zhu, Z., Pathirage, M., Wang, W., Troemner, M., Cusatis, G., 2022. Lattice discrete particle modeling of concrete under cyclic tension–compression with multi-axial confinement. Constr. Build. Mater. 352, 128985.